

Research Article

<https://doi.org/10.1631/jzus.A2200134>



Model test of the mechanism underpinning water-and-mud inrush disasters during tunnel excavation in sandstone and slate interbedded Presinian strata

Peng XU^{1,2}, Peng PENG^{1,2}, Rong-hua WEI^{1,2}, Zhi-qiang ZHANG^{1,2}✉

¹School of Civil Engineering, Southwest Jiaotong University, Chengdu 610031, China

²Key Laboratory of Transportation Tunnel Engineering, Ministry of Education, Southwest Jiaotong University, Chengdu 610031, China

Abstract: Water-and-mud inrush disasters have become a major challenge in underground engineering for the construction of tunnels in sandstone and slate interbedded Presinian strata. Disaster prediction and prevention rely in part on realistic modeling and observation of the disaster process, as well as the identification and examination of the underlying mechanisms. Based on the geological conditions and the historical records of the Xiping Tunnel on the China–Laos Railway, an engineering geological model of the water-and-mud inrush was established. A physical model test that accurately reproduced water-and-mud inrush during tunnel excavation in sandstone and slate interbedded strata was also carried out. Then, testing was conducted that examined the stress and strain, seepage pressure, and high-leakage flow of the surrounding rock. The results indicated that the water-and-mud inrush proceeded through three stages: seepage stage, high-leakage flow stage, and attenuation stage. In essence, the disaster was a catastrophic process, during which the water-resistant stratum was reduced to a critical safety thickness, a water-inrush channel formed, and the water-resistant stratum gradually failed under the influence of excavation unloading and in situ stress–seepage coupling. Parameters such as the stress and strain, seepage pressure, and flow of the surrounding rock had evident stage-related features during water-and-mud inrush, and their variation indicated the formation, development, and evolution of the disaster. As the tunnel face advanced, the trend of the stress–strain curve of the surrounding rock shifted from sluggish to rapid in its speed of increase. The characteristics of strain energy density revealed the erosion and weakening effect of groundwater on the surrounding rock. The seepage pressure and the thickness of the water-resistant stratum had a positive linear relationship, and the flow and thickness a negative linear relationship. There was a pivotal point at which the seepage pressure changed from high to low and the flow shifted from low to high. The thickness of the water-resistant stratum corresponding to the pivotal point was deemed the critical safety thickness.

Key words: Water-and-mud inrush; Sandstone and slate interbedded Presinian strata; Model test; Evolution law; Thickness of water-resistant stratum; Inducing mechanism

1 Introduction

With the introduction of the New Western Development Strategy and Belt and Road Policy, the focus of China's modern traffic engineering has gradually shifted to southwestern mountainous areas with extremely complex geological conditions. The sandstone and slate interbedded Presinian strata are extremely ancient and widely distributed in Southwest China.

Many tunnels are being built in this region. Tunnel construction can result in water-and-mud inrush (Fan et al., 2018). Water-and-mud inrush disasters may cause significant scheduling delays in construction, economic loss, environmental damage, and casualties, all of which may lead to a project being abandoned or redesigned for a new location (Li LP et al., 2016). This has become a significant technological problem that has restricted tunnel construction in Southwest China (Ma et al., 2016; Wang et al., 2019). Therefore, for disaster control and prevention, it is of great scientific value and engineering significance to study the mechanisms inducing water-and-mud inrush events.

✉ Zhi-qiang ZHANG, clark@swjtu.edu.cn

 Zhi-qiang ZHANG, <https://orcid.org/0000-0002-0051-8745>

Received Mar. 15, 2022; Revision accepted July 14, 2022;
Crosschecked Oct. 18, 2022

© Zhejiang University Press 2022

The inrush of water and mud during tunnel construction can be attributed to a combination of factors, including the geological environment, construction disturbances, and external loads, and occurs as a result of multiple stress mechanisms that result in seepage and damage. Theoretical and numerical simulations have been conducted by researchers worldwide to examine and mitigate the associated risks. Wu et al. (2017) selected a series of detection lines on a karst tunnel plane and obtained the corresponding velocity before water inrush in the tunnel and the subsequent pressure change curves, through numerical simulation. Zhao et al. (2018) also used numerical simulation to study the migration law of water inrush in three fault structures under different initial velocities and dynamic viscosities, and identified the causes of water inrush in fault tunnels. Yang WM et al. (2019a) analyzed the fluid-solid coupling between groundwater and the surrounding rock during tunnel excavation using the finite element method, and were able to summarize the pattern regularity of water inrush disasters. Yang et al. (2020a) developed a four-component numerical method to assess the effect of internal soil erosion on the stress state, initial soil density, and initial fine grain size based on continuous medium theory. Yang J et al. (2019b) investigated the effects of coupling between erosion and filtration by simulating a 1D internal erosion test. Yang J et al. (2019a) used a finite element approach to numerically solve an elasto-plastic intrinsic model of a sandy-powdered soil mixture. This was used to monitor the effect of the evolution of porosity and fines content caused by internal erosion on the behaviour of the soil skeleton. Yang et al. (2020b) developed an elasto-plastic principal structure model of a sand-powder soil mixture. They analyzed the different damage modes of an embankment subjected to internal erosion caused by leakage at the base of the foundation under different boundary conditions according to a 3D finite element program. Wang et al. (2020) used the critical water-pressure theory of hydraulic fracturing and numerical simulations to study the process of collapse of surrounding rock under water pressure. Xue et al. (2021) discussed the causes of water-and-mud inrush in real-world scenarios, analyzed the evolution of water-and-mud inrush based on numerical simulation results, and suggested prevention methods. Li et al. (2021) predicted the potential water-bearing area of the Jingzhai Tunnel (on

the China–Laos Railway) using an electromagnetic method, and used numerical simulations to study the mechanism of water inrush and seepage transformation caused by excavation disturbances. Yang et al. (2022) investigated the effect of soil permeability on ground deformation by developing a novel coupled water-force modelling approach based on mixture theory.

Numerical simulations need to limit the mechanical parameters, flow patterns, and constitutive modelling. However, when water-and-mud inrush disasters occur in a real-world tunnel, the fields of stress, displacement, and seepage in the surrounding rock vary broadly, which makes them hard to reproduce and calculate in theoretical models. Physical models, however, can more accurately depict the spatial link between the geological body and the tunnel, as well as the catastrophic process of water-and-mud inrush, all of which are critical in predicting and preventing underground engineering disasters. Liang et al. (2016) analyzed the variations in stress, displacement, and water pressure fields during tunnel excavation using water inrush modelling combined with engineering examples and related theories, and established risk criteria for water inrush. Li SC et al. (2016) monitored the vault displacement, water pressure, and area of excavation disturbance in a fault tunnel section using a physical model, and studied the mechanisms promoting water inrush in cross-fault tunnels. Jiang et al. (2017) used a series of geological disaster models involving water inrush to study the effects of the formation pressure, water pressure, and safety thickness of surrounding rock on water inrush disasters. Zhang et al. (2017) simulated the process of crack formation and hidden fault expansion as well as the evolution of a high water-pressure channel under a mining site. They found that the lagging water inrush was the result of fluid-solid coupling between cracks in the coal floor and tectonic rock zones. Yang WM et al. (2019b) developed a model for water inrush in tunnels with high ground stress and high-water pressure and found that the seepage and stress of the rock mass in the water-resistant layer changed significantly before the occurrence of water inrush. Li et al. (2019) monitored the displacement, stress, and seepage pressures of different monitoring sections in a true triaxial geomechanical model and obtained data from multiple physical responses involved in the surrounding rock failure and resultant water inrush. Yang WM et al. (2019c)

analyzed a model of water inrush failure in an impermeable rock mass and estimated the variation in the displacement, stress, and seepage pressures of the surrounding rock. Pan et al. (2019) studied the stability of surrounding rock in the process of karst tunnel excavation using a 3D model. Their study revealed the mechanism of water inrush and the variation of displacement and water pressure in the failure zone during construction.

Most studies have focused on the causes and patterns of water-and-mud inrush disasters in karst tunnels and cross-fault tunnels, but there has been little research into the causes of these disasters in Presinian strata. Therefore, based on the recently completed Xinping Tunnel built on the China–Laos Railway, we developed a model to reproduce the sandstone and slate interbedded Presinian strata and the entire process of water-and-mud inrush, after developing a fluid-solid coupling with geologically similar materials. We analyzed the variation in the stress and seepage fields of the surrounding rock during tunnel excavation and provided an experimental basis for future research into the mechanisms underpinning water-and-mud inrush disasters. The knowledge gained will contribute to the prevention and mitigation of underground engineering disasters.

2 Xinping Tunnel: description, geology, and disasters

2.1 Project overview

The Yuxi–Mohan (Yumo) Railway is an electrified railway in Yunnan Province, China, which connects Yuxi City with Mohan Port in Mengla County. It is an essential portion of the Trans-Asian Railway. The Yumo Railway is a hallmark project of China's Belt and Road initiative, with a total length of 507 km and a maximum train speed of 160 km/h. A total of 93 tunnels were designed for the Yumo Railway, with a total length of 398 km. The Xinping Tunnel is the key control project for the entire line and had some of the most complex geological conditions. It was classified as a class I “high-risk” tunnel in which water-and-mud inrush disasters occur frequently during construction. The Xinping Tunnel is located in Xinping County, Yuxi City, Yunnan Province. Its entrance mileage marker is D1K46+290 and its exit mileage

marker is D1K61+120. With a total length of 14.8 km, it is a single-entrance, double-line, super-long tunnel. Fig. 1 depicts the topographic plan of the Xinping Tunnel.

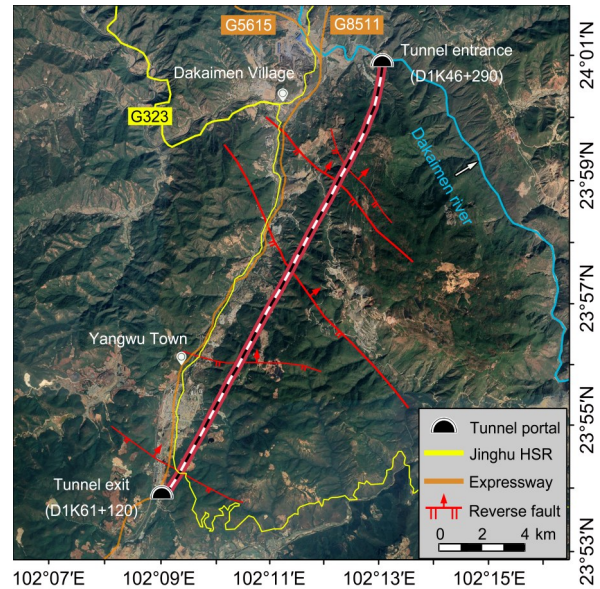


Fig. 1 Topographic plan of the Xinping Tunnel. HSR represents the high-speed railway

The Xinping Tunnel was excavated using a three-bench method with an excavation width of 12.8 m, a height of 11.6 m, and a cross-sectional area of 122 m². A total of eight auxiliary channels were set, including six transverse galleries, one inclined shaft, and one parallel heading. Fig. 2 is an illustration of a cross-section of the Xinping Tunnel.

2.2 Geological features of Presinian strata

The Xinping Tunnel is located in the middle of the Yunnan Plateau, northeast of the Ailao Mountain area, which belongs to a tectonically eroded low-middle mountain landform with complex topography, high mountains, and deep valleys. The Xinping Tunnel passes through Mopan Mountain, in the direction SW210° and at a maximum buried depth of 578 m. The average buried depth of the tunnel is around 270 m, while the height of groundwater head is between 40 and 60 m. A geological cross-section of the Xinping Tunnel is shown in Fig. 2, and the strata are listed in Table 1. The Xinping Tunnel passes mainly through Triassic and Presinian strata. Most of the tunnel is located in the sandstone and slate interbedded Presinian strata of the Heishantou Formation of the Kunyang Group

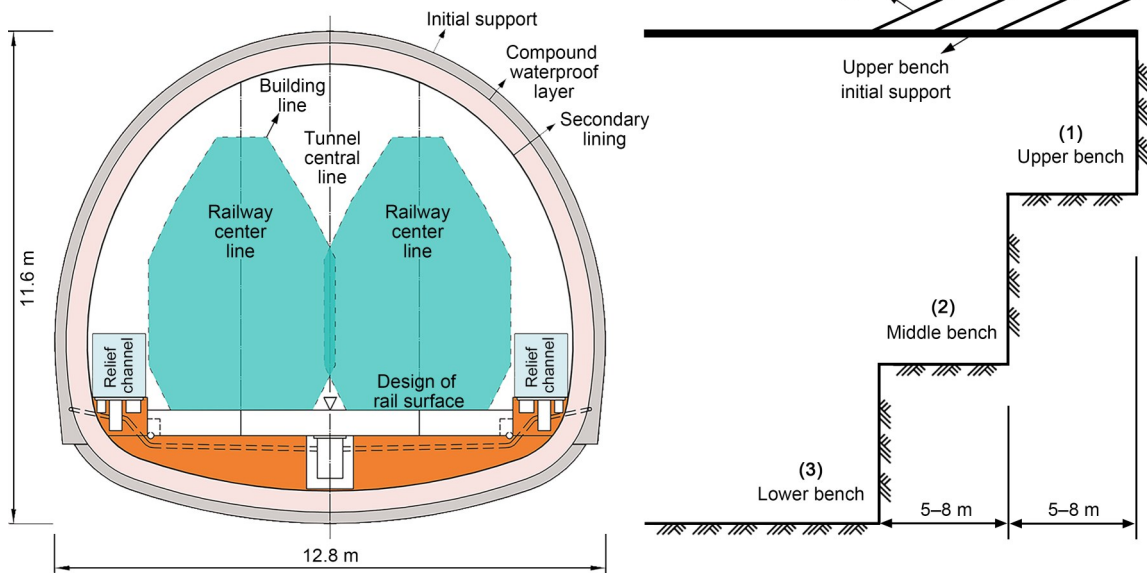


Fig. 2 Diagram of a cross-section of the Xinping Tunnel and the three-bench method

Table 1 Table of strata

Code	Period	Formation	Main lithology
T ₃ g	Triassic	Ganhaizi	Carbonaceous shale
Pt ₁ f	Presinian	Fuliangpeng	Tuff, slate interbedded with sandstone
Pt ₁ d	Presinian	Dalongkou	Limestone, dolomite, slate
Pt ₁ hs ^f	Presinian	Heishantou (member 6)	Slate interbedded with sandstone
Pt ₁ hs	Presinian	Heishantou	Slate interbedded with sandstone

(Pt₁hs), which is also the segment with the highest frequency of water-and-mud inrush disasters (D1K51+290 to D1K59+290 in Fig. 3). The geological structure of the tunnel site was highly developed. The Xinping Tunnel lies between the Shiping–Jianshui fault zone and the Yangwu–Qinglongchang fault zone, parallel to the Yangwu–Qinglongchang fault zone. It passes through seven large and several small structures including the Lukuishan syncline, Xinzhai anticline, Xinzhai reverse fault, Dakaimen–Xinzhai reverse fault, Xiemo reverse fault, Yangwu–Zhaomike reverse fault, and Abudu reverse fault.

The sandstone and slate interbedded Presinian strata are a kind of monoclinial, bedded structure composed of groups of slate and sandstone strata with dip angles of 20°–35°. The thickness of a single slate stratum varies from thin to medium, ranging from 0.1 to 0.5 m. The thickness of a single sandstone stratum varies from medium to thick, ranging from 0.5 to 1.0 m. There are three primary sets of joints growing in the strata, including J1 (N55°E/NW45°–60°), J2

(N45°W/SW40°–50°), and J3 (N65°E/SE40°–45°). The joint spacing is typically 0.1–0.5 m, and the rock integrity coefficient K_v is about 0.30. This suggests that there is a high degree of damage to the integrity of the formation, and the overall strength of the formation is poor. The strata are controlled by weak structural planes and have poor stability. The sandstone and slate interbedded Presinian strata that were exposed during tunnel construction are shown in Fig. 4. The general condition of the strata exposed by the tunnel face was characterized by interlayer wrinkling of the sandstone and slate interbedded strata, which had been affected by tectonic activity and structural planes. The strata were broken into fragments, showing the layered cataclastic structure.

Fig. 5 shows drilling cores of the sandstone and slate interbedded Presinian strata. The overlaying and underlying slate had weak integrity and self-stabilization capabilities based on the core characteristics. The sandstone core was highly fractured, revealing a fragmented structure (rock quality designation RQD=0), and there

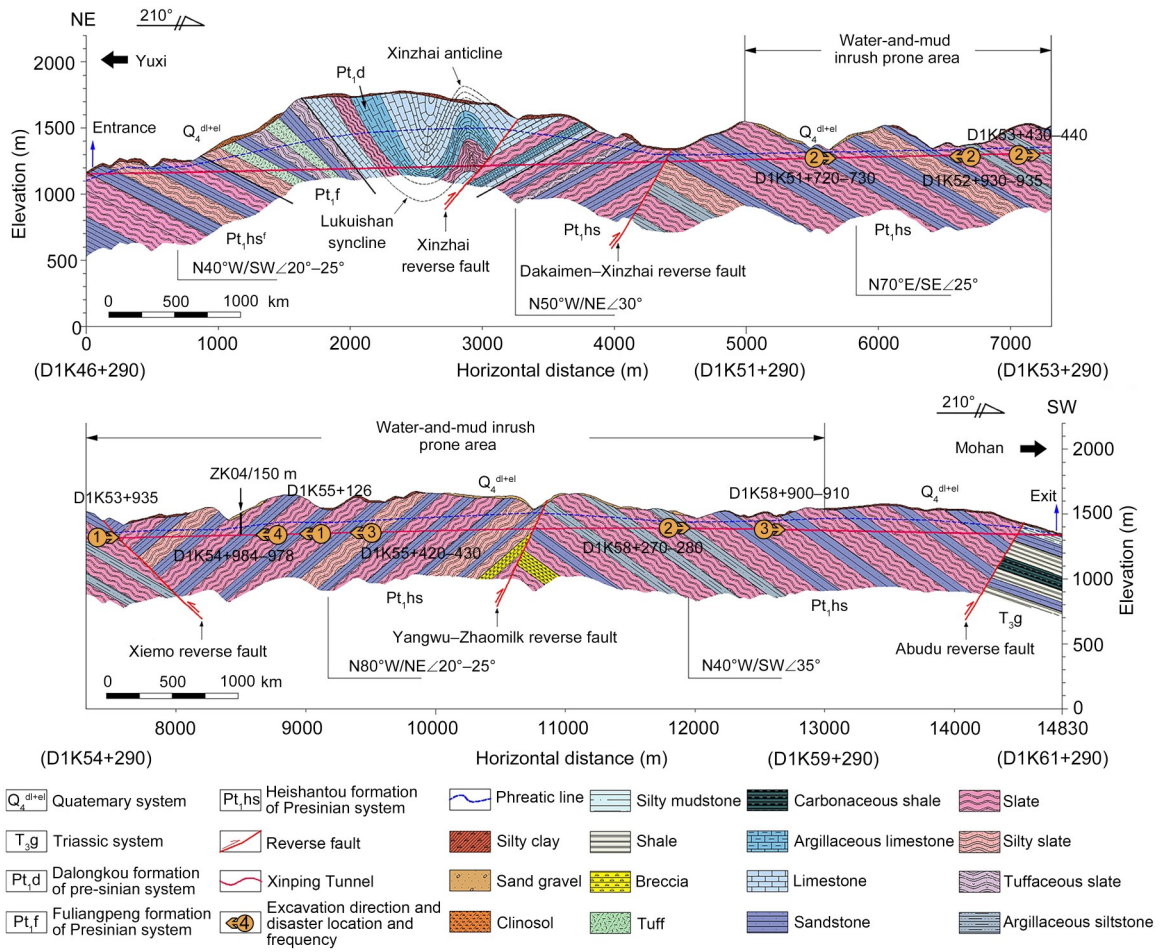


Fig. 3 Longitudinal geological profile of the Xinping Tunnel

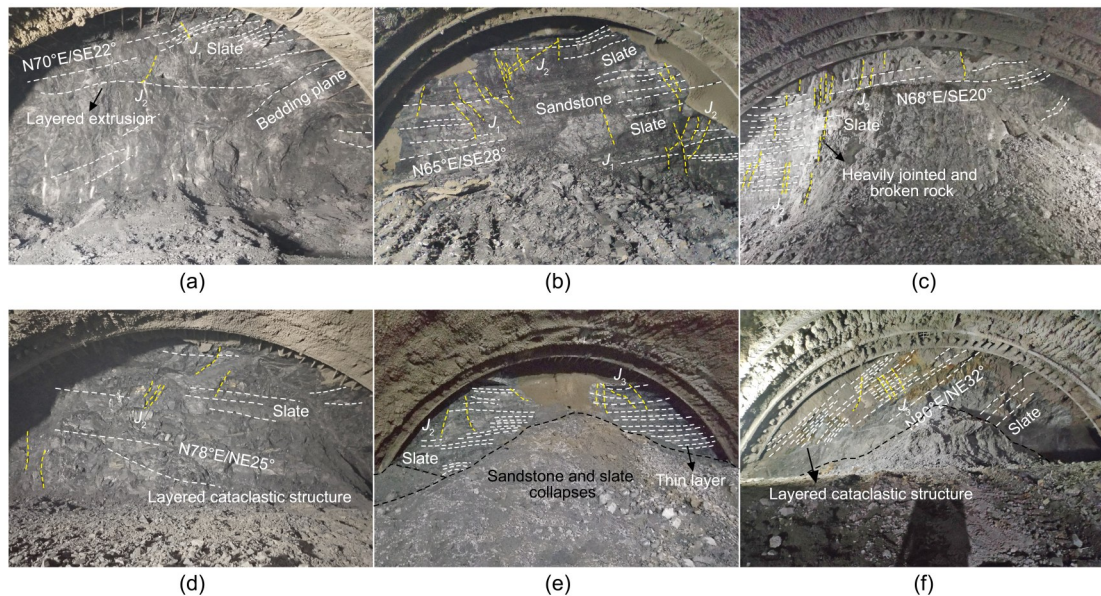


Fig. 4 Geological survey of various tunnel faces: (a) D1K51+478; (b) D1K52+136; (c) D1K53+345; (d) D1K54+310; (e) D1K55+519.4; (f) D1K56+120

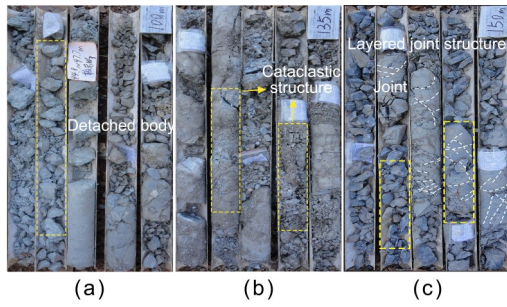


Fig. 5 Core photographs of sandstone and slate interbedded Presinian strata: (a) 94.8–97.7 m, overlying slate; (b) 97.7–138.2 m, sandstone aquifer; (c) 138.2–155.7 m, underlying slate

was little core recovery. Experimental measures of the physical and mechanical properties of the slate and sandstone in the Presinian strata are shown in Table 2 (Choo and Ong, 2020).

Generally, fractures close gradually as the depth increases in the distribution area of monocline, bedded strata. As a result, as depth increases, the water-richness of the strata declines, and the water-richness of deep interlayer fissures is often poor. However, the thick sandstone layer of the Presinian strata has abundant voids and joints, good connectivity and permeability, and the basic conditions to accommodate groundwater. These features are conducive to groundwater flow and storage in the sandstone layer. Therefore, the sandstone strata could be considered the water-bearing stratum. The slate layer, which has closed fissures and low water permeability, provides favorable geological conditions for groundwater collection and storage in the sandstone layer. Consequently, the slate strata were considered the water-resistant stratum. The monoclinic bedded water-bearing structure is formed by the combination of a sandstone water-bearing stratum and a slate water-resistant stratum, and has been the source of water-and-mud inrush disasters. In terms of permeability of the entire structure, the permeability coefficient of the monoclinic bedded water-bearing structure is large in the direction parallel to the bedded plane, but small in the direction perpendicular to the bedded

plane, which shows its anisotropic characteristics (Ong et al., 2022). Groundwater in monoclinic, bedded water-bearing structures is supplied mostly by atmospheric rainfall or surface water through the exposed part of the sandstone layer.

2.3 Cases of water-and-mud inrush disasters

According to on-site records, the Xinping Tunnel has had 41 water-and-mud inrush disasters since its construction, with a total mud inrush of $6.7 \times 10^4 \text{ m}^3$ (including 20 in the main tunnel and 21 in auxiliary channels). From the D1K54+984 to the D1K54+978 mileage marker, there have been four successive water-and-mud inrush disasters, all of which were caused by the typical monoclinic, bedded water-bearing structure. The disaster scenes are shown in Fig. 6. The sandstone water-bearing stratum had been exposed at the D1K54+982 mileage marker with a flow rate of $2.52 \text{ m}^3/\text{h}$, and the dip of the strata in the section corresponded to the direction of tunnel excavation.

(a) The first water-and-mud inrush occurred at the D1K54+982 mileage marker on Dec. 8, 2017, with a mud inrush volume of 300 m^3 .

(b) The second large-scale water-and-mud inrush occurred on the right side of the vault at the same mileage marker on Dec. 12, 2017. A vast volume of dirt and water poured out in a billow-like fashion. The inverted trestle was pushed backward about 30 m, with a cumulative mud inrush of about 3000 m^3 and a maximum water inflow of about $141 \text{ m}^3/\text{h}$.

(c) The third water-and-mud inrush occurred at the D1K54+980 mileage marker on Dec. 22, 2017. The maximum water inflow was $219 \text{ m}^3/\text{h}$, while the mud inrush volume was around 7000 m^3 . The inrush material was a mixture of gray/yellow soil and sand.

(d) The fourth water-and-mud inrush occurred at the D1K54+980 mileage marker on Jan. 19, 2018.

The first mud inrush at the same mileage marker had been relatively small, and the sand mixture had filled and blocked the water-and-mud inrush channel. As construction progressed, the filling materials were

Table 2 Physical and mechanical parameters of slate and sandstone (Choo and Ong, 2020)

Type	Physical parameter				Mechanical parameter				
	ω (%)	RQD	γ (kN/m ³)	k ($\times 10^{-5}$ cm/s)	E (GPa)	c (MPa)	φ (°)	σ_t (MPa)	μ
Slate	0.2	25–30	27.0	1.16	3.10	0.20	19.0	18.0	0.16
Sandstone	5.4	0	20.0	957	–	0.10	30.0	–	0.25

ω is the water content; γ is the bulk density; k is the permeability coefficient; E is the elastic modulus; c is the cohesion forces; φ is the internal friction angle; σ_t is the uniaxial compressive strength; μ is Poisson's ratio

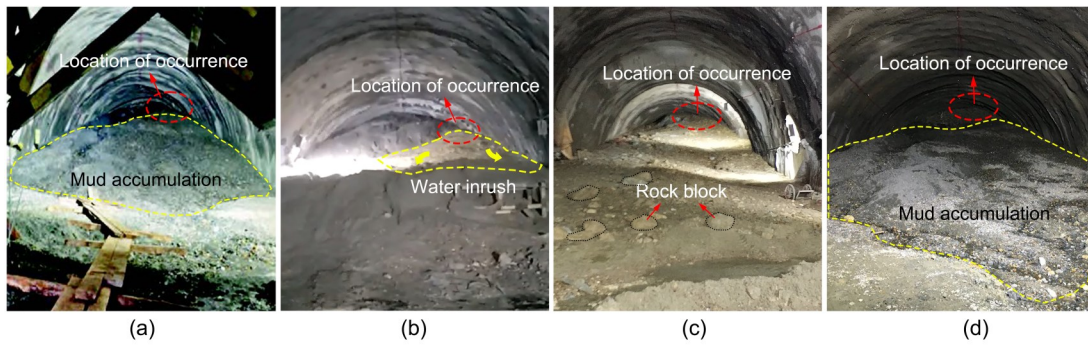


Fig. 6 Scenes from the water-and-mud inrush disasters in the Xinping Tunnel with sandstone and slate interbedded strata: (a) Dec. 8, 2017; (b) Dec. 12, 2017; (c) Dec. 22, 2017; (d) Jan. 19, 2018

washed away due to strong seepage pressure and excavation unloading, and the water-and-mud inrush channel reopened, resulting in the second water-and-mud inrush disaster, significantly greater than the first. The water-and-mud inrush disaster occurred beyond the excavation contour above the vault of the tunnel face, despite the relevant geophysical exploration and drilling verification that had been completed before the disaster. There were one-sided and blind-detection regions, and the geophysical scanning and drilling areas had been arranged in a linear or dot shape, which was insufficient to properly reflect the actual rock surrounding the tunnel.

The water-and-mud inrush disaster in the sandstone and slate interbedded Presinian strata occurred as a result of the monoclinal, bedded water-bearing structure and the underground engineering activities. The scale of the disaster was determined by the water-bearing structure, but the direct cause was the underground engineering activity. Therefore, an engineering geological model of water-and-mud inrush in the Xinping Tunnel was established to study the inrush risks and causal factors based on the geological conditions and historical records (Fig. 7).

3 Design of model test

3.1 Similarity requirements

Physical models must satisfy a series of requirements to ensure the essential similarity between the physical model and the prototype. Similarity is considered in terms of various factors such as the geometry, equilibrium and physical equations, boundary conditions, and Newton’s second law. In this study, a

reduced dimension scale C_L of 80 and a reduced density scale C_γ of 1 were used in the model. The essential similarities between the modeling materials and the undisturbed surrounding rock are summarized in Table 3 according to the similarity theory introduced by Li et al. (2020) and Xu et al. (2021). These similarity criteria set the requirements for the modeling

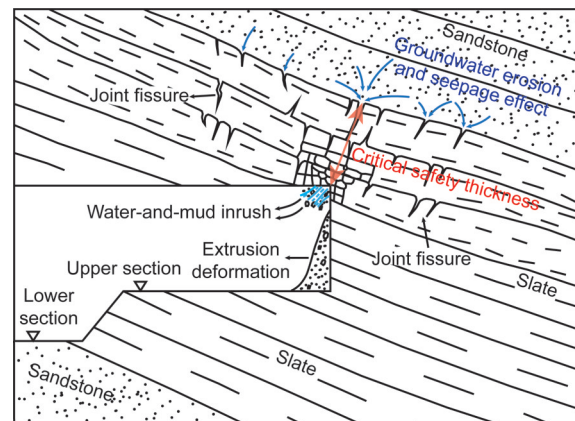


Fig. 7 Engineering geological model of the Xinping Tunnel and water-and-mud inrush

Table 3 Reduced scales of the parameters adopted in the test model

Parameter	Definition	Relation	Reduced scale
Length	$C_L=L_p/L_m$	$C_L=C_L$	80
Density	$C_\gamma=\gamma_p/\gamma_m$	$C_\gamma=C_d/C_L$	1
Permeability coefficient	$C_k=k_p/k_m$	$C_k=\sqrt{C_L}/C_\gamma$	8.94
Elastic modulus	$C_E=E_p/E_m$	$C_E=C_d/C_e$	80
Poisson’s ratio	$C_\mu=\mu_p/\mu_m$	$C_\mu=C_e$	1
Cohesion	$C_c=c_p/c_m$	$C_c=C_\sigma$	80
Stress	$C_\sigma=\sigma_p/\sigma_m$	$C_\sigma=C_\gamma C_L$	80
Strain	$C_\epsilon=\epsilon_p/\epsilon_m$	$C_\epsilon=C_\mu$	1

materials, such as their specified physical and mechanical properties, test model proportions and size, boundary conditions, and values of the initial stress. Herein, the subscript “p” represents the prototype, and “m” represents the test model.

3.2 Model testing system

The model testing system is the main component of testing operation and control. A visualized model testing system of water-and-mud inrush was independently designed for this study (Fig. 8). It had three components: a model test bench, a water supply device, and a data collection system.

3.2.1 Model test bench

A transparent box structure was used to construct the test bench with a steel plate at the bottom and high-strength acrylic plates on four sides. The test bench had a height of 1000 mm, a width of 600 mm, and a length of 400 mm (equivalent to the excavation length of 32 m in the Xinping Tunnel). The size was designed according to the geometric similarity ratio (1:80) of the model. The upper and middle parts of the acrylic plates were reinforced with angled iron stiffeners, and the joints were sealed with glass glue to meet the requirements of stiffness, strength, and sealing. The acrylic plates had four $\Phi 10$ -mm holes on each side. The water-guide hole was on the left, and the lead hole was on the right. The tunnel section was simplified to a circular section that was 160 mm in diameter (corresponding to the 12.8-m diameter of the Xinping Tunnel). The center of the tunnel was 250 mm from the

bottom and 300 mm from the left and right sides. Fig. 9 shows a schematic diagram of the model test bench.

3.2.2 Water supply device

The water supply device was 3 m high and composed of a steel truss, a flexible water tank, and an aqueduct. The flexible water tank was lifted and lowered by a chain hoist. The outlet hole at the bottom of the water supply device was connected to the water-guide holes on the left side of the test bench by a hose to produce a stable groundwater environment and provide variable head heights for the model test. Fig. 10 shows a physical figure of the lifting device.

3.2.3 Data collection system

Resistance microsensors were used to track the stress, strain, and seepage pressures of the surrounding rock during tunnel excavation. A dynamic and static strain test analyzer was used to collect and analyze the data during the test. The aqueduct and measuring cylinder were used to collect and measure the flow, respectively. A camera was positioned in front of the test bench at a predetermined distance to record the dynamic change of the surrounding rock during tunnel excavation and the water-and-mud inrush. The data collection system is shown in Fig. 11.

3.3 Similar materials

For this experiment, using appropriate similar materials was key to achieving an accurate simulation. As the mechanical and hydraulic properties of slate and sandstone are very different, it was necessary to

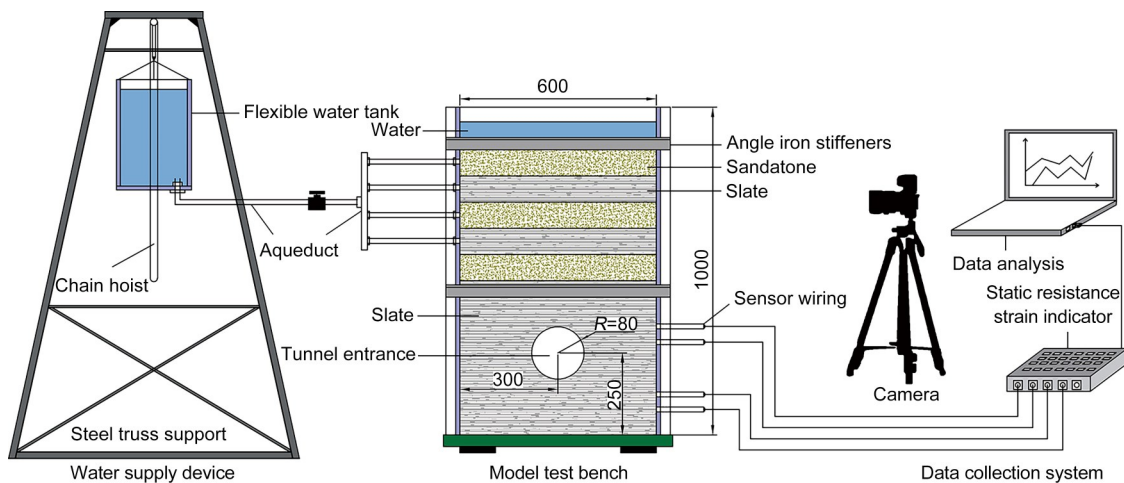


Fig. 8 Design of the model test system of water-and-mud inrush (unit: mm). R is the radius of the tunnel

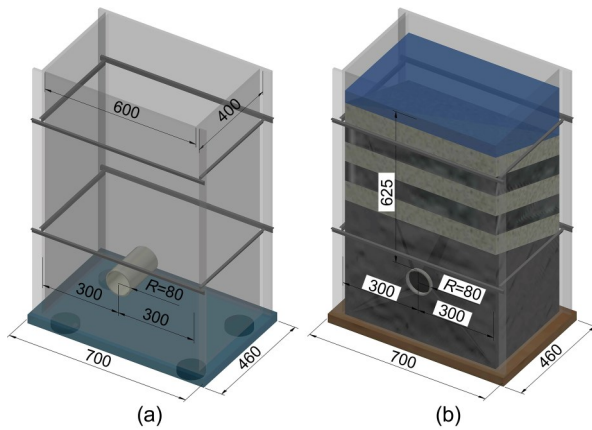


Fig. 9 Model test bench (unit: mm): (a) before loading materials; (b) after loading materials



Fig. 10 Water supply device

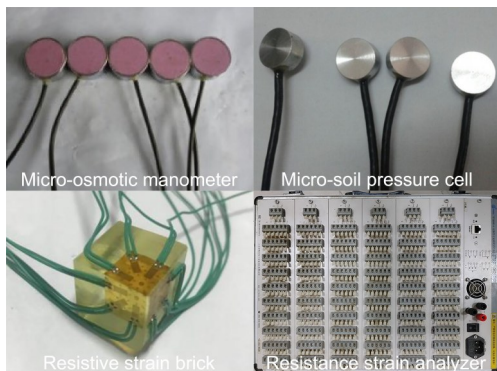


Fig. 11 Data collection system

prepare two types of similar materials. Materials analogous to slate would have low permeability, a low softening coefficient, and low strength, but had to be able to maintain their own strength under water and soil

pressure, whereas materials analogous to sandstone would have high permeability and would disintegrate rapidly under groundwater action.

3.3.1 Slate-like materials

Clay and fine sand were selected as aggregate. To manufacture slate-like materials, fiberglass with low water absorption was used as a binder, and water as a regulator. The above materials were combined into standard specimens in different proportions, and their bulk density γ , elastic modulus E , Poisson's ratio μ , compressive strength σ_c , cohesion c , internal friction angle φ , and permeability coefficient k were measured by laboratory tests. The preparation process is shown in Fig. 12. The preparation of clay, fine sand, fiberglass, and water in a mass ratio of 1:1.5:0.02:0.5 met the basic conditions of low permeability and steady performance of slate-like materials, according to ratio tests. The parameters of the slate-like materials are shown in Table 4.

3.3.2 Sandstone-like materials

The original sandstone rock was broken and could not self-stabilize; therefore, it was prone to collapse under water. Three types of quartz sand with various particle sizes were selected as aggregate, including coarse quartz sand ($0.5 \text{ mm} \leq d < 5.0 \text{ mm}$), medium quartz sand ($0.25 \text{ mm} \leq d < 0.50 \text{ mm}$), and fine quartz sand ($0.075 \text{ mm} \leq d < 0.250 \text{ mm}$). Gypsum was chosen as a binder, as it collapses easily under water. Our ratio experiments found that the ideal mass ratio of coarse sand, medium sand, fine sand, and gypsum was 1:1.3:0.7:0.1. Fig. 13 depicts the preparation process for sandstone-like materials, and Table 5 lists the parameters.

3.4 Model test scheme

The simulation range for the model test of the Xinping Tunnel was from mileage markers D1K54+990 to D1K54+958 (corresponding to the 400-mm length of the model test bench) with a groundwater level of 50 m (equivalent to 625 mm of the model size). Fig. 14 shows a diagram of the test's structure, in which the size was translated using a geometric similarity ratio. In the test, the tunnel was located in the slate stratum, and the overlying strata were monoclinical, bedded strata of slate intercalated with sandstone. The stratum height was 44 m (corresponding to

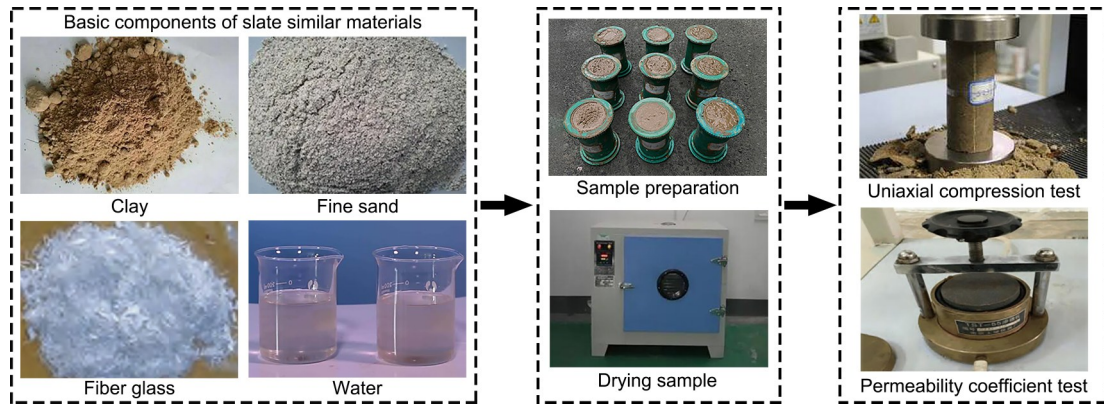


Fig. 12 Development of slate-like materials

Table 4 Physical and mechanical parameters of slate and similar materials

Type	γ (kN/m ³)	E (GPa)	c (MPa)	φ (°)	σ_c (MPa)	μ	k ($\times 10^{-5}$ cm/s)
Slate	27.0	3.10	0.200	19.0	18.0	0.16	1.16
Similar materials	26.5	0.04	0.003	18.0	0.23	0.16	0.13

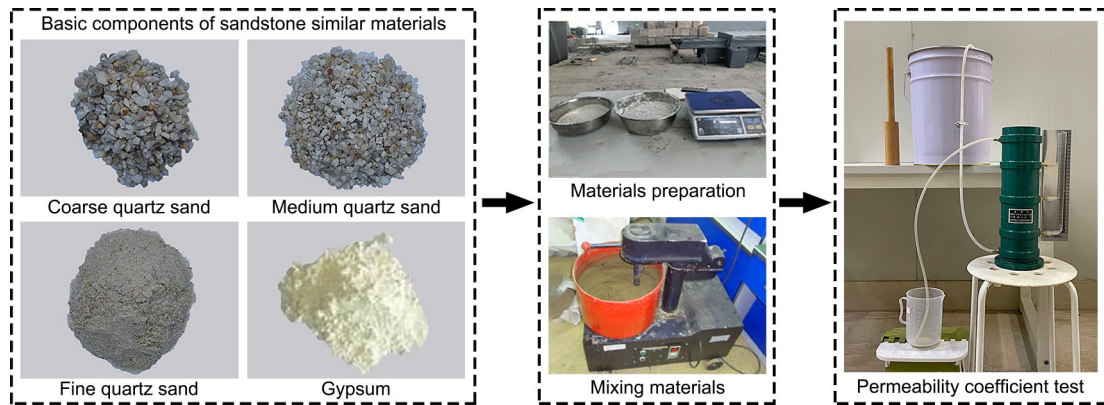


Fig. 13 Development of sandstone-like materials

Table 5 Hydrological properties of sandstone and similar materials

Type	γ (kN/m ³)	c (MPa)	φ (°)	μ	k ($\times 10^{-3}$ cm/s)
Sandstone	20.0	0.100	30.0	0.25	9.57
Similar materials	19.0	0.001	28.0	0.21	1.07

the 550 mm in Fig. 14), and the dip angle was 20°, which was the same as the direction of tunnel excavation. The slate stratum was regarded as the water-resistant stratum, and the sandstone stratum as the water-bearing stratum. The thickness of the water-resistant stratum was defined as the distance between the floor of the first sandstone water-bearing stratum and the vault of the tunnel. The maximum thickness of the water-resistant stratum $L_m=136.8$ mm before

tunnel excavation, corresponded to the actual thickness of 10.9 m of the water-resistant stratum.

Micro-soil pressure cells, resistive strain bricks, and micro-osmotic manometers were used in this experiment to measure stress, strain, and seepage pressures, respectively, in real time at various locations in the surrounding rock. The key section monitoring method was used in the test. The first half of the tunnel was considered the key region to monitor given the size limitations of the simulation and the impact of integrating excessive monitoring parameters into the analysis. The layout of the monitoring section is shown in Fig. 15. Three monitoring sections were selected for this test, among which monitoring sections I and III were located at $X=100$ and 200 mm in front of the tunnel, respectively, to monitor the seepage pressure

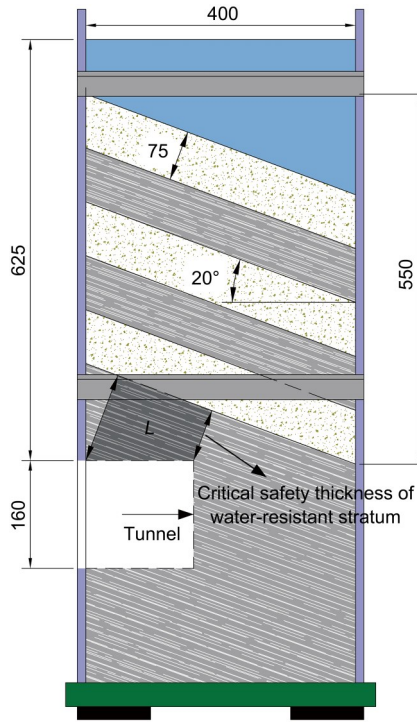


Fig. 14 Model test structure diagram (unit: mm)

of the surrounding rock. Each monitoring section contained five micro-osmotic manometers. Outside the vault, measuring points P_1 (P_6) and P_2 (P_7) were spaced 50 and 100 mm apart, respectively. P_3 (P_8) and P_4 (P_9) were located at 50 and 100 mm outside the spandrel, respectively. The measuring points, which included P_5 (P_{10}), were spaced 50 mm apart on the Y -axis (the measuring points in brackets represent the monitoring points in monitoring section III). Monitoring section II was located at $X=120$ mm in front of the tunnel, and micro-soil pressure cells and resistive strain bricks were buried at 100 mm on the vault and the spandrel, respectively. All the measuring points of all monitoring sections were in the slate stratum, except P_7 . The measuring point P_7 at monitoring section III in the vault was located in the sandstone stratum.

3.5 Model construction and tunnel excavation process

The primary steps in the construction of the model and the excavation of the tunnel were as follows:

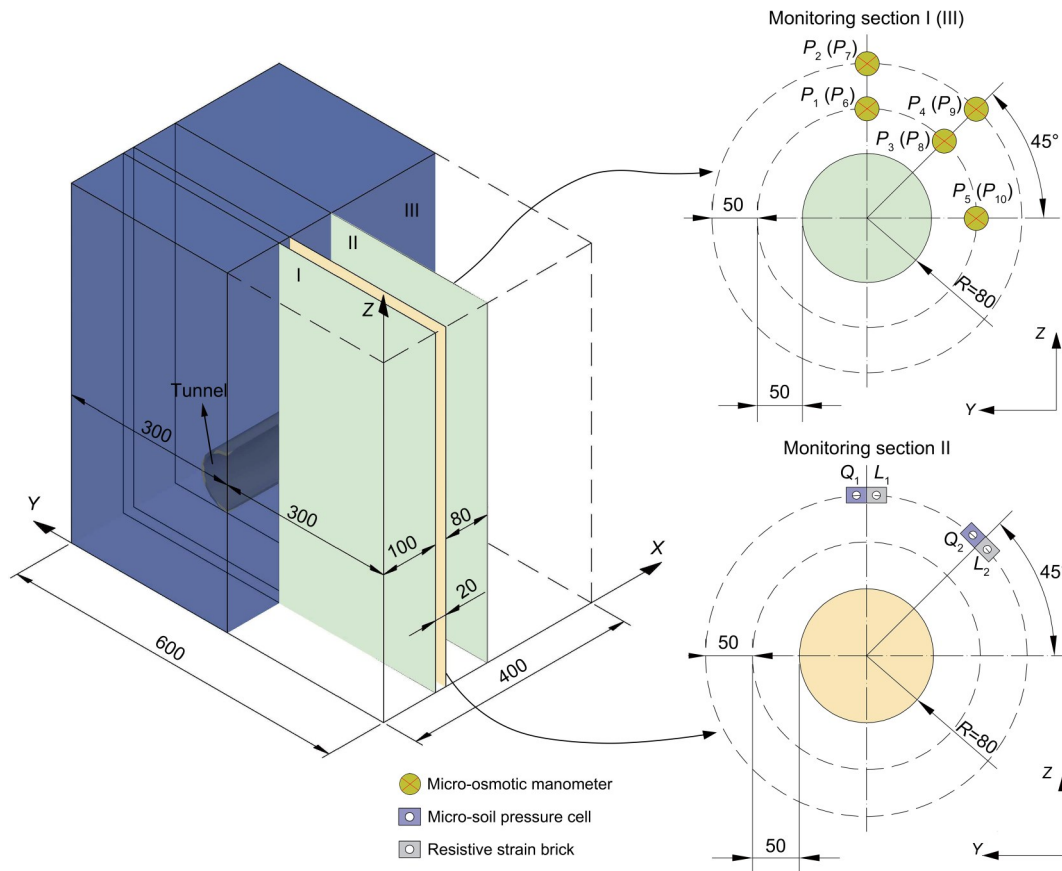


Fig. 15 Distribution of monitoring points in the model test (unit: mm)

(1) Similar material preparation and model filling: The model was filled with layers of the prepared materials to simulate the real-world conditions. Evenly mixed materials were poured into the test box in layers at an incline of 20° . For the strata above the tunnel, the filling height of slate and sandstone was 75 mm. The model body's density was then strictly controlled by the material quality and filling height. Roughening between layers was essential during the paving of similar materials. We were careful to avoid disturbing the monitoring elements in the strata and to prevent the formation of natural seepage channels when tamping down the materials.

(2) Placement of monitoring components: Each monitoring component was buried at the specified location and position during the material-filling process. Measurement lines were drawn from the lead hole and connected to the dynamic and static strain analyzer.

(3) Setting up the water-enriched environment: The water supply device was activated so that the sandstone stratum would be fully saturated with water. The water flow was paused when the groundwater level reached the design height, and the model body was then left static for 48 h to stabilize the tunnel's stress and seepage fields.

(4) Tunnel excavation: The tunnel was excavated by manual drilling, using the three-bench method. The excavation length was fixed at 200 mm (corresponding to an excavation length of 16 m in the real tunnel), and the length of each excavation footage was 20 mm (corresponding to the actual excavation length of 1.6 m). A total of 24 excavation steps were scheduled. The height of the upper bench was 50 mm (corresponding to the actual height of 4.0 m of the upper bench), the height of the middle bench was 60 mm (corresponding to the actual height of 4.8 m of the middle bench), and the height of the lower bench was 50 mm (corresponding to the actual height of 4.0 m of the lower bench). Excavation was halted when the footage length had been reached. The excavation depth was then recorded and the thickness of the water-resistant stratum calculated in real time. Excavation of the next footage length was conducted after the data of each monitoring element had been stabilized. The groundwater level was maintained at a constant level during tunnel excavation. If there was a significant change in monitoring data or water seepage at the excavation surface during excavation, excavation was

immediately stopped, and the state of the tunnel face was monitored in real time during the water-and-mud inrush process.

4 Results and analysis of the model test

4.1 Analysis of the water-and-mud inrush process

Fig. 16 represents the process and phenomena of water-and-mud inrush in the model test.

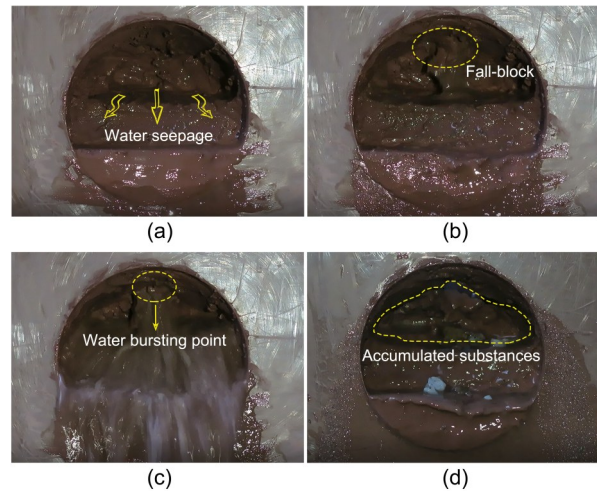


Fig. 16 Catastrophic process of water-and-mud inrush: (a) water seepage in the tunnel face; (b) increased water seepage; (c) water-and-mud inrush; (d) end of water-and-mud inrush

The process of water-and-mud inrush was separated into three stages based on the experimental characteristics and features.

(1) Seepage stage: When the upper bench had been excavated to a depth of $X=90$ mm (corresponding to the thickness of the water-resistant stratum $L=106$ mm), new micro-fissures were generated in the surrounding rock, existing fissures were expanded, and a tiny amount of water seepage developed on the vault. However, as the tunnel face advanced, the water seepage channel closed, and the water seepage of the vault disappeared briefly. When the upper bench was excavated to the position of $X=120$ mm (corresponding to the thickness of the water-resistant stratum $L=95.7$ mm), the water seepage channel expanded again, and the water seepage on the vault increased (Fig. 16a), due to the combined action of surrounding rock unloading, the water and soil pressure, and the groundwater permeability.

(2) High-leakage flow stage: When the upper bench had been excavated to the point of $X=150$ mm (corresponding to the thickness of the water-resistant stratum $L=85.5$ mm), the water seepage of the vault switched to a runoff state. Meanwhile, on the vault, a water-conducting channel developed and released a stream of dirty water. At this point, the excavation was halted. The water-conducting channel grew as a result of the seepage–stress coupling, and sandstone debris was removed by the underground flow. The rock surrounding the vault fell and even collapsed in parts, followed by a minimal flow of mud (Fig. 16b). The water-conducting channel eventually became integrated and further damaged the surrounding rock on the vault leading to a water-and-mud inrush disaster, with a large amount of water–sand mixture gushing into the tunnel from the vault. The water-and-mud inrush is shown in Fig. 16c. Although the occurrence of the water-and-mud inrush was sudden, the water-conducting channel experienced a long process of infiltration damage from expansion to connection.

(3) Attenuation stage: The magnitude of the disaster and the flow of water-and-mud inrush steadily diminished over time, and the water quality gradually changed from turbid to limpid. The water-and-mud inrush stopped when the overlying sandstone had completely discharged all of its groundwater, which was not efficiently replenished. In the end, a substantial volume of sand mixture accumulated at the tunnel face (Fig. 16d).

To facilitate a clearer and intuitive understanding of the process and phenomena of the model test, the excavation length and the thickness of the water-resistant stratum at key excavation steps are summarized in Table 6, as well as experimental phenomena. The corresponding actual dimensions are included.

4.2 Stress–strain variation characteristics

The stability of the surrounding rock is reflected by the variation in strength after structural failure and weakening. As a result, the stress–strain curve of the surrounding rock during tunnel excavation was used to assess the stability characteristics. Fig. 17 shows the stress–strain curves of the tunnel vault and spandrel of monitoring section II, with the strain energy density of the surrounding rock represented by the area under the stress–strain curve.

(1) The stress–strain curve of the vault showed an increasing trend during tunnel excavation from $X=0$ to 90 mm (Fig. 17). There was an initial in-situ stress of 6.5 kPa in both the vault and spandrel due to the influence of overlying water and soil pressure. The vault's stress was rapidly released, and the excavation disturbed the surrounding rock, causing stress redistribution. As the tunnel face advanced, the stress–strain curve of the vault had a slow-to-quick growth trend as the vault's stress shifted rapidly from low to high. The water-conducting channel extended and connected when the tunnel had been excavated to $X=150$ mm, causing water-and-mud inrush. Any changes in vault stress were insignificant when the strain increased. The stress–strain curves on the vault and the spandrel showed a similar response, but the vault reached critical failure stress at $X=150$ mm, before the spandrel.

(2) The stable states of surrounding rocks varied depending on their stress conditions. To some extent, the strain energy density of the surrounding rock reflected its stability. Therefore, as the strain energy density increased, the stability of the surrounding rock weakened. In this case, there was a significant possibility of water-and-mud inrush. The strain energy density of the vault was 20.7% more than that of the spandrel, according to an examination of strain energy

Table 6 Description of model test process

Excavation step	Model dimension		Actual dimension		Phenomenon description
	Excavation length (mm)	L (mm)	Excavation length (m)	L' (m)	
4	60	116.3	4.8	9.3	Tunnel surrounding rock was stable without obvious change
6	90	106.0	7.2	8.5	Tiny amount of water seepage developed on the vault
10	120	95.7	9.6	7.6	Water seepage on the vault increased
13	150	85.5	12.0	6.8	Water seepage of the vault switched to a runoff state

L represents the thickness of the water-resistant stratum at the model scale; L' represents the actual thickness of the water-resistant stratum

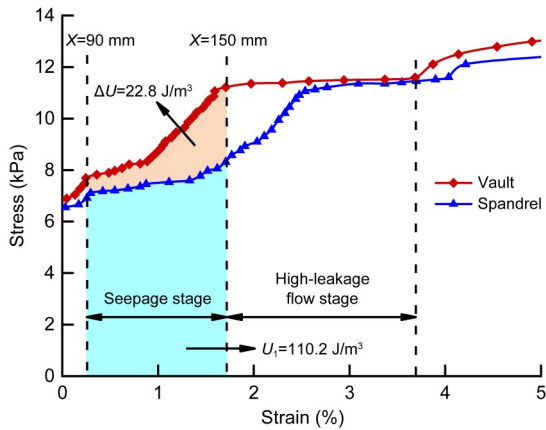


Fig. 17 Stress–strain curves during tunnel excavation. ΔU is the difference of strain energy density between vault and spandrel; U_1 is the strain energy density of spandrel

density at the location of the water-and-mud inrush. This conclusion was supported by the position of the water-and-mud inrush on the tunnel vault.

4.3 Variation characteristics of the seepage field

Figs. 18 and 19 demonstrate the variable features of seepage pressure and flow in monitoring sections I and III at various excavation distances.

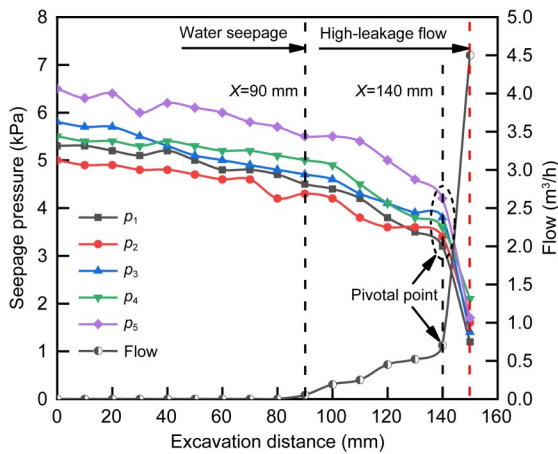


Fig. 18 Characteristic curves of seepage pressure and flow at different excavation distances of monitoring section I

(1) In general, as tunnel excavation distance increased, the change trend of seepage pressure at each monitoring site followed a similar pattern, namely, a slow reduction, then a rapid reduction, and finally, an abrupt change. However, the trend of the flow gradually shifted from stable and constant to gradually increasing, until suddenly altering.

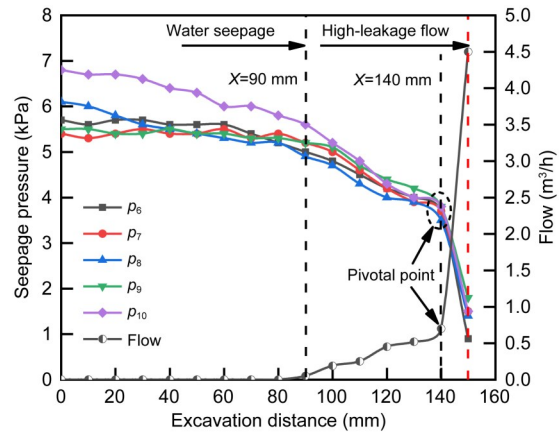


Fig. 19 Characteristic curves of seepage pressure and flow at different excavation distances of monitoring section III

(2) The sandstone and slate interbedded strata were in a stable seepage field before tunnel excavation. When tunnel excavation began, the excavation disturbance and unloading of the surrounding rock caused the tunnel seepage field to alter, and the seepage pressure gradually decreased. The flow increased from zero as the tunnel was excavated to $X=90$ mm, suggesting that initiation and development of fissures in the surrounding rock led to an increase in the water seepage capacity. The continuous expansion of surrounding rock fissures provided a water seepage channel for groundwater as the tunnel face reached $X=140$ mm, which in turn increased the seepage failure. At each monitoring site, the flow and seepage pressure changed abruptly. When the tunnel was excavated to $X=150$ mm, a water-and-mud inrush disaster occurred, and the flow instantly increased from 0.7 to 4.5 m^3/h , a 5.4-fold increase. The seepage pressure at monitoring points P_1 and P_6 of the vault decreased the most, by 62.5% and 75.7%, respectively. This change was brief and rapid, and the range in variation of the seepage pressure and flow was large, which was consistent with the features of strong concealment and then sudden and powerful destruction caused by the water-and-mud inrush disasters in the Xinping Tunnel.

4.4 Effect of water-resistant stratum thickness

The water-resistant stratum was the final barrier preventing a water-and-mud inrush disaster, and its thickness determined whether or not a disaster would occur. To determine the influence of the thickness of the water-resistant stratum on the evolution characteristics of seepage pressure and flow during tunnel excavation,

monitoring data from P_1 , P_3 , and P_5 of monitoring section I and P_6 , P_8 , and P_{10} of monitoring section III were selected to draw the relationship curves among the seepage pressure, the flow, and the thickness of the water-resistant stratum (Fig. 20).

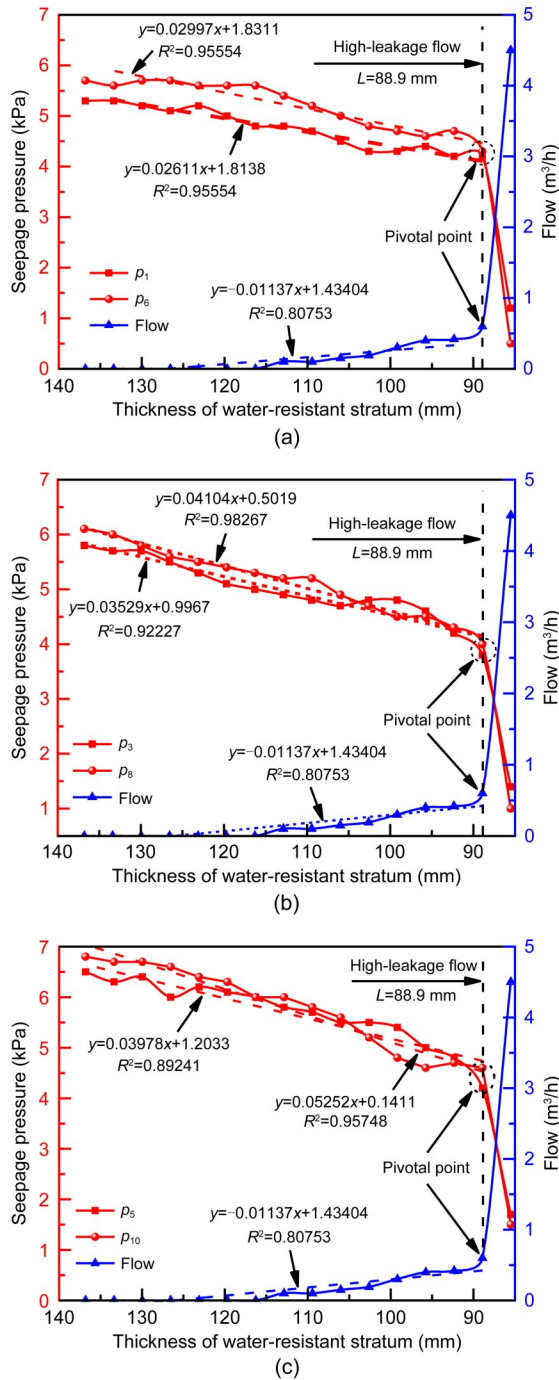


Fig. 20 Relationships among seepage pressure, flow, and the thickness of water-resistant strata: (a) monitoring points P_1 and P_6 ; (b) monitoring points P_3 and P_8 ; (c) monitoring points P_5 and P_{10}

Before tunnel excavation, the initial thickness of the water-resistant stratum was 136.8 mm (corresponding to the actual maximum thickness of 10.9 m of the water-resistant stratum). When the water-and-mud inrush disaster occurred, the thickness was 85.5 mm (corresponding to the actual thickness of 6.8 m of the water-resistant stratum). The thickness of the water-resistant stratum had a positive linear relationship with the seepage pressure and a negative linear relationship with the flow at each monitoring station. With the reduction in thickness, the seepage pressure gradually dropped. The fitted linear correlation coefficients between the seepage pressure and the thickness of the water-resistant stratum were greater than 0.8. These results suggest that the initial fracture and the new fracture expanded more easily as the thickness of the water-resistant stratum was reduced. The permeability resistance of the surrounding rock reduced over time, as did the bearing capability of the rock against the water and soil pressure. The seepage pressure of the surrounding rock abruptly altered as the thickness of the water-resistant stratum was reduced to the critical safety thickness. At this point, only a small amount of seepage pressure was required to destroy the water-resistant stratum, resulting in the water-and-mud inrush.

Fig. 21 further shows the relationship between the seepage pressure and the flow of the surrounding rock when the thickness of the water-resistant stratum was reduced. There was a negative correlation between seepage pressure and flow, as well as two highly concentrated regions: a “high-seepage pressure and low-flow” area and a “low-seepage pressure and high-flow” area. In other words, both seepage pressure and flow had a pivotal point where the seepage pressure decreased from high to low, and the flow rose from low to high. This point was regarded as the characteristic point of deterioration of the water-resistant stratum, and the thickness of the water-resistant stratum corresponding to this point was the critical safety thickness. In the model test, the critical safety thickness of the water-resistant stratum was 88.9 mm (corresponding to the actual critical thickness of 7.1 m of the water-resistant stratum).

There was a good linear relationship between the seepage pressure and the flow, which indicated that the seepage process of the model test conformed with Darcy’s law. Therefore, the permeability coefficient

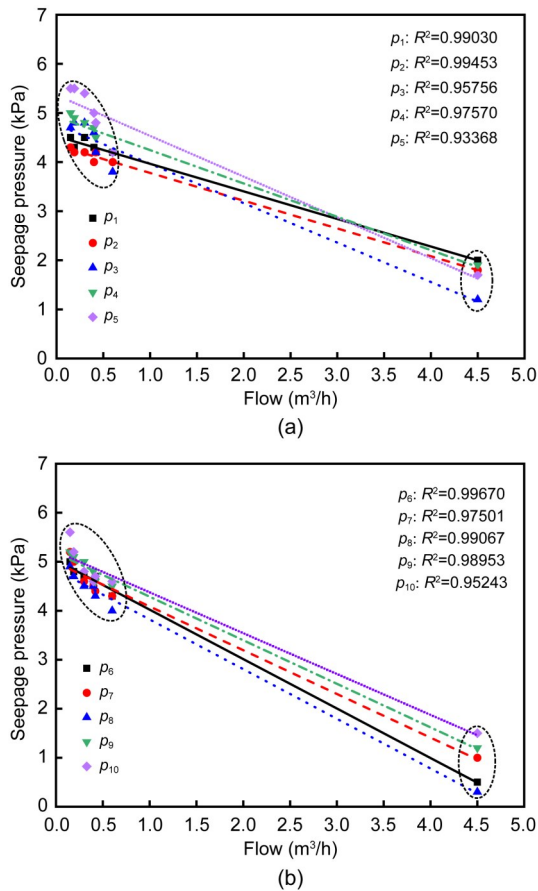


Fig. 21 Relationships between the seepage pressure and flow of each monitoring section: (a) monitoring section I; (b) monitoring section III

and hydraulic gradient of the surrounding rock could be calculated according to Darcy's law. Fig. 22 showed the change rule of hydraulic gradient and permeability coefficient of the surrounding rock (monitoring sections I and III) during the reduction of the thickness of the water-resistant stratum. The variation curves of the hydraulic gradient and permeability coefficient both showed obvious segmental characteristics with the decrease of the thickness of the water-resistant stratum (Fig. 22). Before the high-leakage flow, with the decrease of the thickness of the water-resistant stratum, the hydraulic gradient changed slightly and the permeability coefficient was basically unchanged. After the high-leakage flow, the hydraulic gradient decreased sharply, while the permeability coefficient increased rapidly. Therefore, after the thickness of the water-resistant stratum was reduced to the critical safety thickness, the permeability coefficient of the surrounding rock increased rapidly, the hydraulic

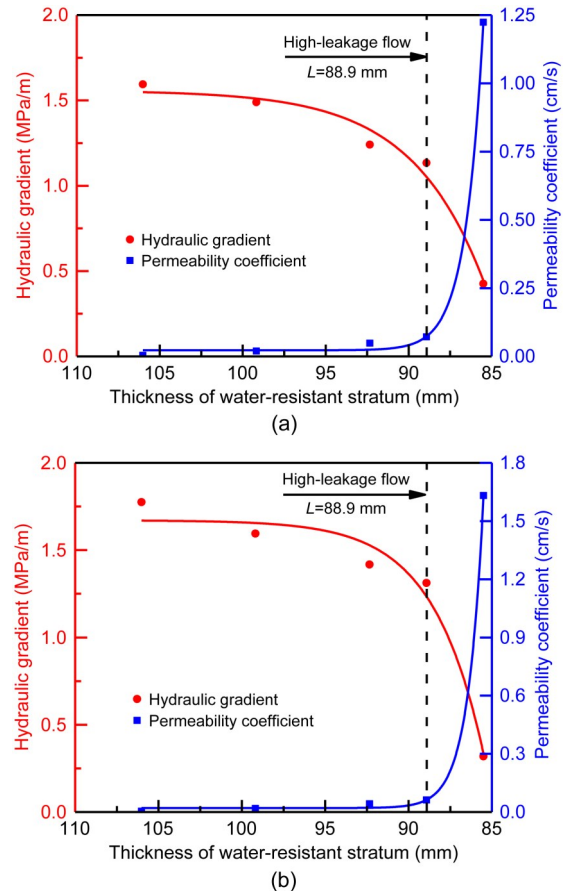


Fig. 22 Change rule of hydraulic gradient and permeability coefficient: (a) monitoring section I; (b) monitoring section III

gradient decreased sharply, the water-resistant capacity of the surrounding rock decreased sharply, and the surrounding rock was damaged by seepage. The smaller the thickness of water-resistant stratum, the greater the risk of water-and-mud inrush. The process of the water-and-mud inrush is an evolutionary process in which the water-resistant stratum gradually loses its water-resistant capacity.

5 Conclusions

In this study, we examined the mechanisms underpinning water-and-mud inrush disasters during the construction of tunnels in sandstone and slate interbedded Presinian strata. A physical model test was conducted based on the water-and-mud inrush disasters in the Xinping Tunnel on the China-Laos Railway. The main conclusions were as follows:

(1) An engineering geological model in sandstone and slate interbedded Presinian strata was built based on the engineering characteristics and geological conditions of the Xinping Tunnel. Materials similar to slate and sandstone that matched the test requirements were developed. The model test successfully reproduced the process of water-and-mud inrush in the field of practical engineering.

(2) The process of water-and-mud inrush in sandstone and slate interbedded Presinian strata was divided into three stages: seepage stage, high-leakage flow stage, and attenuation stage. In the process of the water-and-mud inrush, parameters such as the stress-strain, seepage pressure, and flow of the surrounding rock had stage-related characteristics, which indicated the disaster's formation, development, and evolution.

(3) As the tunnel face advanced, the trend of the stress-strain curve of the surrounding rock increased from slow to steep, and the characteristics of strain energy density revealed the erosion and weakening effect of groundwater on the surrounding rock. The strain energy density of the vault was 20.7% higher than that of the spandrel at the seepage stage. As the strain energy density of the surrounding rock increased, the surrounding rock weakened, and the risk of water-and-mud inrush due to seepage failure increased.

(4) The seepage pressure had a positive linear relationship while the flow had a negative linear relationship with the thickness of the water-resistant stratum. In the process of changing seepage pressure and flow, there was a pivotal point. Before this point, the formation of the high-leakage flow channel had a slow seepage failure process. The permeability pressure of the surrounding rock reduced significantly after the pivotal point, whereas the permeability coefficient of the water-resistant stratum rapidly increased. The pivotal point was regarded as the characteristic point of deterioration of the water-resistant stratum, and the thickness of the water-resistant stratum corresponding to this point was determined to be the critical safety thickness. The critical safety thickness of the water-resistant stratum was 88.9 mm in the model test.

(5) The water-and-mud inrush disaster of a tunnel in sandstone and slate interbedded Presinian strata was related not only to the properties of the surrounding rock, but also to the excavation disturbance and groundwater action. The water-and-mud inrush is a catastrophic process induced by the action of excavation

unloading and in situ stress-seepage coupling, in which the water-resistant stratum reaches the critical safety thickness, a high-leakage flow channel forms, and the water-resistant stratum gradually fails.

Acknowledgments

This work is supported by the National High-Speed Rail United Foundation of China (No. U1934213).

Author contributions

Peng XU and Zhi-qiang ZHANG designed the research. Peng XU and Peng PENG were responsible for the model test and paper writing. Rong-hua WEI processed the corresponding data. Zhi-qiang ZHANG helped to organize the manuscript. Peng XU revised and edited the final version.

Conflict of interest

Peng XU, Peng PENG, Rong-hua WEI, and Zhi-qiang ZHANG declare that they have no conflict of interest.

References

- Choo CS, Ong DEL, 2020. Assessment of non-linear rock strength parameters for the estimation of pipe-jacking forces. Part 2. *Numerical modeling. Engineering Geology*, 265:105405.
<https://doi.org/10.1016/j.enggeo.2019.105405>
- Fan HB, Zhang YH, He SY, et al., 2018. Hazards and treatment of karst tunneling in Qinling-Daba mountainous area: overview and lessons learnt from Yichang-Wanzhou Railway system. *Environmental Earth Sciences*, 77(19):679.
<https://doi.org/10.1007/s12665-018-7860-1>
- Jiang HM, Li L, Rong XL, et al., 2017. Model test to investigate waterproof-resistant slab minimum safety thickness for water inrush geohazards. *Tunnelling and Underground Space Technology*, 62:35-42.
<https://doi.org/10.1016/j.tust.2016.11.004>
- Li G, Ma WB, Tian SM, et al., 2021. Groundwater inrush control and parameters optimization of curtain grouting reinforcement for the Jingzhai Tunnel. *Geofluids*, 2021: 6634513.
<https://doi.org/10.1155/2021/6634513>
- Li LP, Tu WF, Shi SS, et al., 2016. Mechanism of water inrush in tunnel construction in karst area. *Geomatics, Natural Hazards and Risk*, 7(S1):35-46.
<https://doi.org/10.1080/19475705.2016.1181342>
- Li LP, Sun SQ, Wang J, et al., 2020. Experimental study of the precursor information of the water inrush in shield tunnels due to the proximity of a water-filled cave. *International Journal of Rock Mechanics and Mining Sciences*, 130:104320.
<https://doi.org/10.1016/j.ijrmms.2020.104320>
- Li SC, Liu HL, Li LP, et al., 2016. Large scale three-dimensional seepage analysis model test and numerical simulation research on undersea tunnel. *Applied Ocean Research*, 59:510-520.

- <https://doi.org/10.1016/j.apor.2016.07.013>
- Li SC, Gao CL, Zhou ZQ, et al., 2019. Analysis on the precursor information of water inrush in karst tunnels: a true triaxial model test study. *Rock Mechanics and Rock Engineering*, 52(2):373-384.
<https://doi.org/10.1007/s00603-018-1582-2>
- Liang DX, Jiang ZQ, Zhu SY, et al., 2016. Experimental research on water inrush in tunnel construction. *Natural Hazards*, 81(1):467-480.
<https://doi.org/10.1007/s11069-015-2090-2>
- Ma D, Bai HB, Miao XX, et al., 2016. Compaction and seepage properties of crushed limestone particle mixture: an experimental investigation for Ordovician karst collapse pillar groundwater inrush. *Environmental Earth Sciences*, 75(1):11.
<https://doi.org/10.1007/s12665-015-4799-3>
- Ong DEL, Jong SC, Cheng WC, 2022. Ground and groundwater responses due to shaft excavation in organic soils. *Journal of Geotechnical and Geoenvironmental Engineering*, 148(8):05022003.
[https://doi.org/10.1061/\(ASCE\)GT.1943-5606.0002820](https://doi.org/10.1061/(ASCE)GT.1943-5606.0002820)
- Pan DD, Li SC, Xu ZH, et al., 2019. Experimental and numerical study of the water inrush mechanisms of underground tunnels due to the proximity of a water-filled karst cavern. *Bulletin of Engineering Geology and the Environment*, 78(8):6207-6219.
<https://doi.org/10.1007/s10064-019-01491-5>
- Wang J, Li SC, Li LP, et al., 2020. Mechanism of water inrush in fractures and block collapse under hydraulic pressure. *Mathematics and Computers in Simulation*, 177:625-642.
<https://doi.org/10.1016/j.matcom.2020.05.028>
- Wang XT, Li SC, Xu ZH, et al., 2019. Risk assessment of water inrush in karst tunnels excavation based on normal cloud model. *Bulletin of Engineering Geology and the Environment*, 78(5):3783-3798.
<https://doi.org/10.1007/s10064-018-1294-6>
- Wu J, Li SC, Xu ZH, et al., 2017. Flow characteristics and escape-route optimization after water inrush in a backward-excavated karst tunnel. *International Journal of Geomechanics*, 17(4):04016096.
[https://doi.org/10.1061/\(ASCE\)GM.1943-5622.0000787](https://doi.org/10.1061/(ASCE)GM.1943-5622.0000787)
- Xu ZL, Luo YB, Chen JX, et al., 2021. Mechanical properties and reasonable proportioning of similar materials in physical model test of tunnel lining cracking. *Construction and Building Materials*, 300:123960.
<https://doi.org/10.1016/j.conbuildmat.2021.123960>
- Xue YG, Kong FM, Li SC, et al., 2021. Water and mud inrush hazard in underground engineering: genesis, evolution and prevention. *Tunnelling and Underground Space Technology*, 114:103987.
<https://doi.org/10.1016/j.tust.2021.103987>
- Yang J, Yin ZY, Laouafa F, et al., 2019a. Internal erosion in dike-on-foundation modeled by a coupled hydromechanical approach. *International Journal for Numerical and Analytical Methods in Geomechanics*, 43(3):663-683.
<https://doi.org/10.1002/nag.2877>
- Yang J, Yin ZY, Laouafa F, et al., 2019b. Modeling coupled erosion and filtration of fine particles in granular media. *Acta Geotechnica*, 14(6):1615-1627.
<https://doi.org/10.1007/s11440-019-00808-8>
- Yang J, Yin ZY, Laouafa F, et al., 2020a. Hydromechanical modeling of granular soils considering internal erosion. *Canadian Geotechnical Journal*, 57(2):157-172.
<https://doi.org/10.1139/cgj-2018-0653>
- Yang J, Yin ZY, Laouafa F, et al., 2020b. Three-dimensional hydromechanical modeling of internal erosion in dike-on-foundation. *International Journal for Numerical and Analytical Methods in Geomechanics*, 44(8):1200-1218.
<https://doi.org/10.1002/nag.3057>
- Yang J, Yin ZY, Liu YJ, et al., 2022. Multiphysics modelling of backfill grouting in sandy soils during TBM tunneling. *Acta Geotechnica*, in press.
<https://doi.org/10.1007/s11440-022-01528-2>
- Yang WM, Fang ZD, Wang H, et al., 2019a. Analysis on water inrush process of tunnel with large buried depth and high water pressure. *Processes*, 7(3):134.
<https://doi.org/10.3390/pr7030134>
- Yang WM, Yang X, Fang ZD, et al., 2019b. Model test for water inrush caused by karst caves filled with confined water in tunnels. *Arabian Journal of Geosciences*, 12(24):749.
<https://doi.org/10.1007/s12517-019-4907-x>
- Yang WM, Wang MX, Zhou ZQ, et al., 2019c. A true triaxial geomechanical model test apparatus for studying the precursory information of water inrush from impermeable rock mass failure. *Tunnelling and Underground Space Technology*, 93:103078.
<https://doi.org/10.1016/j.tust.2019.103078>
- Zhang SC, Guo WJ, Li YY, et al., 2017. Experimental simulation of fault water inrush channel evolution in a coal mine floor. *Mine Water and the Environment*, 36(3):443-451.
<https://doi.org/10.1007/s10230-017-0433-9>
- Zhao N, Wang YC, Meng B, et al., 2018. Numerical simulation on the seepage properties of soil-rock mixture. *Advances in Materials Science and Engineering*, 2018:1859319.
<https://doi.org/10.1155/2018/1859319>